# Purdue Physics REU/RET conference
# Agenda and Abstracts
# July 31, 2025, room PHYS 242

9:00 Grayson Welch. *Classifying Hamiltonians by M-body entanglement entropy of ground and excited states*. (Dr. Vayrynen)
9:20 Kyle Chessler. *Precise Measurements in Cesium.* (Dr. Elliott)
9:40 Madeline Rehwinkel. *Prospects of Top Quark Entanglement at the High Luminosity Large Hadron Collider (HL-LHC)*. (Dr. Jung)
10:00 Icarus Blum. *Preliminary Characterization of a Superconducting Qubit System.* (Dr. Ma)

10:20 Break

10:30 Aidan Jacobsen. *Kinetic Inductance Measurements of Superconducting Heterostructures*. (Dr. Rokhinson)
10:50 Jordan Sexton. *Simulating Wave Propagation in Fractured Media.* (Dr. Pyrak-Nolte)
11:10 David Lawrence. *Sandstone Fracture Intersections*. (Dr. Pyrak-Nolte)
11:30 Craig Smiley. *Leveraging Online Simulations to Strengthen Specific Points in Students' Understanding in the Physics Curriculum at the Secondary Level.* (Dr. Rebello)

11:50 Lunch break (on your own)

1:00 Eva Clancy. *Investigating Ti-based metal-organic frameworks for applicability in photoelectrochemical cells*. (Dr. Pushkar)
1:20 Sagarika Menon. *Expanding Twistronics to Wafer Scale 2D films*. (Dr. Zhu)
1:40 Patrick Bak. *Development of a Photon Counting System and Co-Sublimation Chamber for DBT-Doped Anthracene Crystal Growth.* (Dr. Hood)

2:00 Break

2:10 Maddy Spark. *Graphene and hBN Encapsulation of 2D FeTeSe for Superconducting Proximity Studies.* (Dr. Chen)
2:30 Zachary Pleska. *Analyzing Remains of Dramatic Stellar Death.* (Dr. Milisavjevic)

2:50 The end

6:00 - *Farewell party/picnic at Sergei Savikhin's house for REU/RET participants Advisors & significant others are welcome, but please reply to confirm attendance.*

# Classifying Hamiltonians by M-body entanglement entropy of ground and excited states

*Grayson Welch[1], Jukka I. Vayrynen[2]*

[1]Taylor University, Department of Physics and Engineering, Upland Indiana

[2]Purdue University, Department of Physics and Astronomy, West Lafayette Indiana

**Introduction** Entanglement entropy is a measure of how correlated one part of a quantum system is with another, possibly providing clues on why macroscopic phenomena are emergent from quantum mechanics. In fermionic systems, M-body entanglement entropy measures these correlations between M particles and the remainder of the system. We developed software to simulate the Hubbard and t-V models and to track changes in M-body entanglement entropy of ground and excited states under different parameters.

**Variable Classification** Here N will refer to the total number of particles in a state, M will refer to the number of particles in a sub-group, D is the total number of sites available for N particles to occupy.

**M-body entanglement entropy** M-body entanglement entropy is calculated by taking the trace of a reduced density matrix. This density matrix is obtained by performing a partial trace over the subsystem we are not interested in. For example, suppose we have a quantum system composed of two subsystems, A and B. In previous work, entanglement entropy has often been computed by tracing out a spatial region (for instance, A could represent the left half of space), which measures quantum correlations between region A and region B. In contrast, M-body entropy quantifies the amount of quantum information shared between a group of M particles and the rest of the system. Calculating the M-body reduced density matrix is equivalent to finding every possible M-body groups of creation and annihilation operators[1].

$$\rho^{M}_{i,j} = [\mathrm{Tr}_{N-M\ldots N}(|\Psi\rangle\langle\Psi|)]_{i,j} = \langle\Psi|c^{\dagger}_{j_1}\ldots c^{\dagger}_{j_M}c_{i_M}\ldots c_{i_1}|\Psi\rangle$$

It should be noted that when the density matrix is diagonal, and all elements are equal, then the state is considered maximally mixed. Here, the von-Neumann entropy is maximized. This means that we can no longer recover the original state from the information we have. The information is "hidden" in entanglement.

$$\hat{\rho}^{M} \propto \mathbb{I}$$

$$S_{\max} = \binom{N}{M}\ln\left[\frac{\binom{\mathrm{D}}{\mathrm{M}}}{\binom{N}{M}}\right]$$

**Models** The primary model used this summer was the Hubbard model. The Hubbard model allows for nearest-neighbor hopping of both spin-up and spin-down particles. When a site is doubly occupied, an interaction energy is incurred. The ground states of this model are known as Mott insulators, which avoid double occupancy of sites. It should be noted that this model does not allow spin flips, which is *crucial* to this presentation!

$$\mathcal{H} = \sum_{i,\sigma}^{\frac{D}{2}} \left( c_{i+1,\sigma}^{\dagger} c_{i,\sigma} + h.c. \right) + U \sum_{i}^{\frac{D}{2}} (\hat{n}_{i,\uparrow} \hat{n}_{i,\downarrow})$$

Another model used this summer was the t-V model. Like the Hubbard model, it allows for nearest-neighbor hopping of fermions. However, this model is spinless, and an interaction energy is incurred when two fermions occupy adjacent sites. The ground states of this model are known as charge density wave, which avoid nearest neighbor occupancy.

$$\mathcal{H} = \sum_{i,\sigma}^{D} \left( c_{i+1}^{\dagger} c_{i} + h.c. \right) + V \sum_{i}^{D} (\hat{n}_{i} \hat{n}_{i+1})$$

**Evolution of single slater states** A critical component of this summer's work was studying the evolution of entropy when an initial Slater determinant was evolved under the Hubbard model. A Slater determinant has the form $c_1^{\dagger} c_2^{\dagger} |0\rangle$ and initially has zero entropy. For the Hubbard model, numerical simulations show that initial states with greater total spin reach an entropic saturation below the upper bound set by the reduced density matrix.

This led us to prove that the density matrix becomes block diagonal when time-evolved states respect certain symmetries of the Hamiltonian. Each block functions as its own density matrix, with its own corresponding upper bound on entropy. By summing these individual upper bounds, we obtained a refined total bound that is lower than the maximum entropy of a fully mixed density matrix.

We also time-evolved states under the t-V model and observed similar behavior. However, since this model is spinless, it raised questions about which symmetries are being conserved. It is hypothesized that the total bond number (i.e., the number of nearest-neighbor fermion pairs) is conserved in the system.

**Analysis of Ground States varying parameters** Another component of this summer's work was studying the entanglement entropy of ground states for various Hamiltonians. While confirming results from previous studies, we also simulated new models in an ongoing effort to identify maximally entangled ground states.

One result we found is that the ground states of the Hubbard model, even as the interaction strength $U$ increases, do not reach maximal entanglement entropy. Furthermore, when examining higher M-body entanglement, numerical simulations show that an even smaller fraction of the maximal entropy is achieved. There are two ideas that might explain this: 1) The locality of the Hubbard model interaction may prevent quantum information from being distributed among particle groups. 2) The ground state's expectation value of total spin is, on average, non-zero, which—as discussed earlier—lowers the upper bound on entropy.

**Regarding maximally M-body entangled ground states** Another member of our group, Irakli Giorgadze, recently derived a proof showing that a maximally M-body entangled ground state can only be realized by an (M+1)- body interacting Hamiltonian. This implies that the Hubbard model can, at most, produce maximal 1-body entanglement. As a result, we began exploring more exotic three-body interaction terms in an effort to generate a maximally entangled 2-body state.

A variety of three-body interaction terms were tested, with limited success. One notable result came from numerically simulating a random interaction term appended to the Hubbard model. In this case, using just 1% of all possible three-body interaction terms produced a maximally entangled ground state. However, the physical relevance of this result remains unclear, as the interaction is highly non-local.

**Future Work**

1. It would be valuable to confirm our hypothesis that energy conservation imposes a bound on entropy in the t-V model. Establishing this could allow us to place additional constraints on the entropic upper bound, deepening our understanding of how system parameters influence entanglement entropy.
2. Introducing a spin-flip term into the Hubbard model may aid in the search for a maximally entangled ground state by breaking total spin conservation. In this scenario, the state $|\Psi\rangle$ would no longer be restricted to a single spin sector, potentially activating off-diagonal blocks in the density matrix and allowing it to achieve a maximally mixed form.

**Acknowledgements**

1. This material is based upon work supported by the National Science Foundation through the Research Experience for Undergraduates program under Grant Number PHY-2244297.
2. I thank the Väyrynen Group at Purdue University for their guidance and support throughout this project.

**Works Cited**

[1]Giorgadze, I., Huang, H., & Gaines, J., et. al. (2025). Characterizing maximally many-body entangled fermionic states by using M-body density matrix. *Quantum*, *9*, 1778. https://doi.org/10.22331/q-2025-06-24-1778.

# Precision Measurements in Cesium

Kyle Chessler[1,2], D.S. Elliott[2,3,4]

[1] *Department of Physics, Hamilton College, Clinton, 13322, New York, USA*
[2] *Department of Physics and Astronomy, Purdue University, West Lafayette, 47909, Indiana, USA*
[3] *Purdue Quantum Science and Engineering Institute, Purdue University, West Lafayette, 47909, Indiana, USA*
[4] *School of Electrical and Computer Engineering, Purdue University, West Layfayette, 47909, Indiana, USA*

July 31, 2025

Transitions between the hyperfine states of cesium are a fertile ground for studying the nuclear weak force due to the phenomenon of atomic parity violation (APV), which is caused by the nuclear weak force, present in these transitions [1]. The Elliott research group specializes in high-resolution spectroscopy to measure these cesium transitions and refine known physics. This summer, I contributed to this body of work by helping to prepare for two measurements, a measurement of an atomic parity violating transition on the ground state of cesium, and a measurement of the Stark shift, which is splitting caused by application of an external electric field [2], on the $8p^2P_J$ state in cesium. For the ground state measurement, any unwanted magnetic fields cause unwanted transitions, suppressing the desired APV signal. To combat this, we plan to install two sets of magnetic sensors to reduce the difficulty of zeroing the magnetic field, and search for drifts. I found appropriate magnetic sensors for this task, and designed a circuit incorporating those sensors. For the Stark shift measurement, I assisted with preparing the apparatus, building a photodiode circuit and a power supply. I also set up a photomultiplier tube that was used to collect data.

## Acknowledgments

This material is based upon work supported by the National Science Foundation through the Research Experience for Undergraduates program under Grant Number PHY-2244297.

## References

1. Safronova, M. *et al.* Search for new physics with atoms and molecules. *Reviews of Modern Physics* **90,** 025008 (2018).
2. Quirk, J. A., Jacobsen, A., Damitz, A., Tanner, C. E. & Elliott, D. Measurement of the Static Stark Shift of the 7s $S^2_{1/2}$ Level in Atomic Cesium. *Physical Review Letters* **132,** 233201 (2024).

# Prospects of Top Quark Entanglement at the High Luminosity Large Hadron Collider (HL-LHC)

Madeline Rehwinkel[1, 2]

[1]Bryn Mawr College | [2]Purdue University

The Large Hadron Collider (LHC) at CERN accelerates protons to immense energy levels and produces collisions of those high-energy protons to probe the conditions at the start of our universe and to discover the fundamental particles that make up our world. As a part of the Compact Muon Solenoid (CMS) experiment at the LHC, the Jung research group investigates the top quark and top antiquark byproducts of the high-energy collisions. A diagram of the CMS subdetectors is provided in Figure 1 [1]. The LHC previously collided protons at a center-of-mass energy of 13 TeV, and a planned upgrade of the collider, called the High Luminosity Large Hadron Collider (LH-LHC), will increase the center-of-mass energy of the collisions to 14 TeV to examine physics at an even higher energy scale [2].

The Jung group is specifically interested in the quantum entanglement present in the byproducts of the collisions in the LHC. Particles are quantum entangled if the state, such as the spin, of one particle is dependent on the state of the other particle. In previous studies about quantum entanglement between top quarks and top antiquarks, entanglement has been observed in the phase space of 345 GeV$< m(t\bar{t}) <$ 400 GeV, where $m(t\bar{t})$ is the invariant mass of the top and antitop quarks [3].

As the heaviest fundamental particle in the Standard Model (SM), top quarks decay too quickly to be detected, however their daughter particles can be detected. Due to their rapid decay, top quarks decay before they can hadronize and lose their spin information.

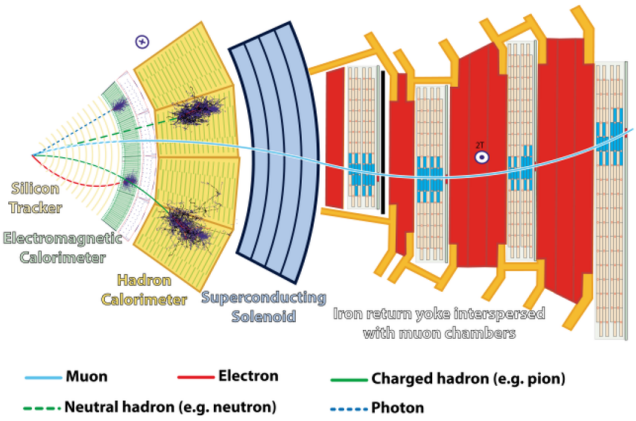


FIG 1. Diagram of the subdetectors in the Compact Muon Solenoid (CMS) experiment detector, from [1]. Different particles will follow different paths due to the varying magnetic fields inside the detector and will be detected and identified by different subdetectors.

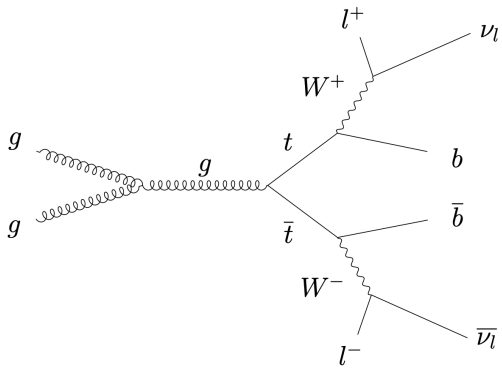


FIG 2. The Feynman diagram of the production and decay process of the top quarks and top antiquarks studied. They are produced through gluon-gluon fusion, and they both decay into leptons. This is described as the dileptonic decay chain [4].

Additionally, if both top quarks decay leptonically, shown in Figure 2, almost 100% of the spin information from the top quarks is passed to the daughter leptons. This allows the spin information of top quarks to be studied by reconstructing the top quarks from the leptons' spin information [4].

The spin-sensitive coefficient D measures the extent of quantum entanglement between the top and antitop quarks. The coefficient D varies from 1 to -1, where entanglement is present in a certain phase space corresponding to -1 < D < -1/3. This coefficient is calculated from equation (1):

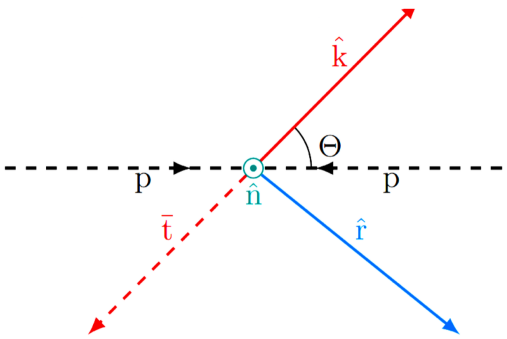


FIG 3. From [4], the definition of the k hat, r hat, and n hat axes for each collision event. The direction of the incoming protons is p and t bar is the direction of scattering of the top antiquark.

$$\frac{1}{\sigma}\frac{d\sigma}{d\,cos\varphi} = -\frac{1}{3}(1 - D\,cos\varphi), \qquad (1)$$

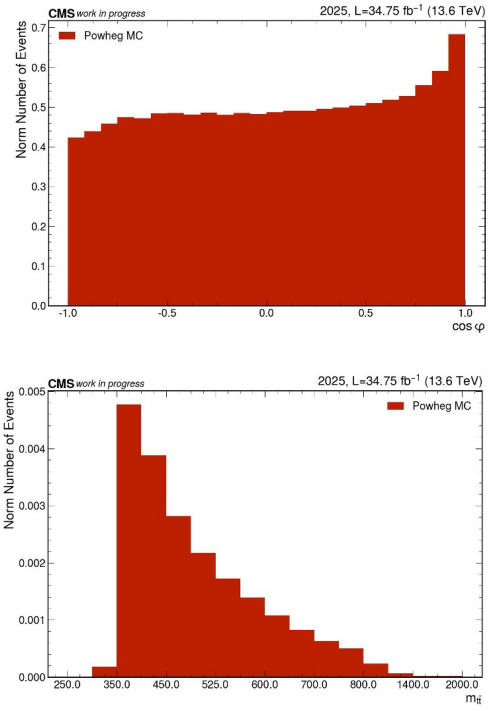


FIG 4. The (a) distribution of cos phi, and the (b) distribution of m(ttbar), both plotted from the data in the new MC file. Both distributions matched expectations and confirmed the validity of the new MC file.

which is derived from the production and decay matrix element for the $t\bar{t}$ system and where $\varphi$ is the angle between the daughter leptons: $cos\varphi = \hat{l}^{+} \cdot \hat{l}^{-}$. The coefficient D can also be calculated with equation (2):

$$D = -\frac{1}{3}tr(C) = -(C_{kk} + C_{rr} + C_{nn})/3, \qquad (2)$$

where $C_{kk}$, $C_{rr}$, and $C_{nn}$ measure the entanglement present along the $\hat{k}$, $\hat{r}$, and $\hat{n}$ axes in the zero momentum frame of the $t\bar{t}$ system defined for each collision by the direction of the incoming protons and the outgoing top quarks [4]. These axes are pictured in Figure 3.

A previous REU student completed a predictive analysis of the quantum entanglement that could be observed in the HL-LHC using a Monte Carlo (MC) simulation of the probabilistic events in the collider. Their analysis incorporated only the nominal sample, and they found entanglement present in the lower $m(t\bar{t})$ phase space for 300 GeV < $m(t\bar{t})$ < 400 GeV.

In my work I am extending the previous analysis to incorporate shape-based systematic

uncertainties. These include the systematic uncertainties introduced by the theoretical modeling differences such as the transverse momentum of the top and antitop quarks ($p_t$), the uncertainty in the parton distribution functions (PDF), the renormalization, as well as experimental (detector) systematic uncertainties such as the jet energy scale (JES) uncertainty, the jet energy resolution (JER) uncertainty. The PDF, renormalization, and $p_t$ uncertainties are projected to be fractions of what they were determined to be in a previous run of the LHC, and the JES and JER uncertainties are determined by a lookup table created by a CMS study [5].

Additionally, I worked with a different MC simulation file than the previous REU student did, so before any analysis could be completed many scripts had to be edited to work with the new file, and later the file itself had to be edited to be used with the existing frameworks. To confirm the validity of the data in the new file, distributions of many observables and spin coefficients were plotted and were found to match expectations. Two of these distributions are graphed in Figure 4.

**Acknowledgements**

I would like to thank Osama Ragab Ahmed Dawood for his supportive guidance and advice throughout my project. Our weekly meetings were an invaluable part of this learning experience. In addition, I would also like to thank Lingqiang He for his support and contributions this summer. Finally, I would like to thank Professor Andreas Jung for his leadership in the laboratory and for providing such an interesting project for me. This work is supported by the National Science Foundation through the Research Experience for Undergraduates program under Grant Number PHY-2244297.

**References**

[1] A. B. Misura, J. Music, M. Prvan, and D. Lelas, “Towards Real-Time Machine Learning-Based Signal/Background Selection in the CMS Detector Using Quantized Neural Networks and Input Data Reduction,” *Applied Sciences*, 14, 1559, 2024. 10.3390/app14041559.

[2] CMS Collaboration, “Projection of the top quark spin correlation measurement and search for top squark pair production at the HL-LHC,” CMS PAS FTR-18-034, Jun, 2022. cds.cern.ch/record/2813262/files/FTR-18-034-pas.pdf.

[3] CMS Collaboration, “The CMS experiment at the CERN LHC,” TOP-23-001, Apr, 2024. cds.cern.ch/record/2893854/files/TOP-23-001-pas.pdf?version=1.

[4] CMS Collaboration, “Differential Measurements of Top Quark Polarizations and Spin Correlations in ttbar Dileptonic Final States from Proton-Proton Collisions at √s = 13 TeV with the CMS Experiment,” *Physical Review D*, 100, 2019. 10.1103/physrevd.100.072002.

[5]A. S. Bakshi, A. Jung, and G. Negro , “Projections of Top Quark Spin Correlations to 14 TeV and 3 ab-1.” (CMS Draft Analysis Note)

# Preliminary Characterization of a Superconducting Qubit System

Icarus Blum[1, 2], Hebah Goderya[2], Alex Ma (PI)[2]

Mount Holyoke College, MA | Purdue University, IN

Quantum computers use quantum bits (qubits) to store and evaluate large amounts of data that would take classical computers a long time to work through (if they even could). A qubit is the smallest possible unit of quantum information, and can be in states of 0, 1, or a superposition of both (Fig 1) [1]. However, qubits don't naturally exist, so we need to artificially create them with two level systems (TLS). For our system, we use transmon qubits, utilizing parallel Josephson Junctions (JJ) (Fig 2) to create SQUIDS (two JJs in a loop where a magnetic flux can be passed to tune the qubits), in conjunction with a capacitor to make the system an anharmonic oscillator.

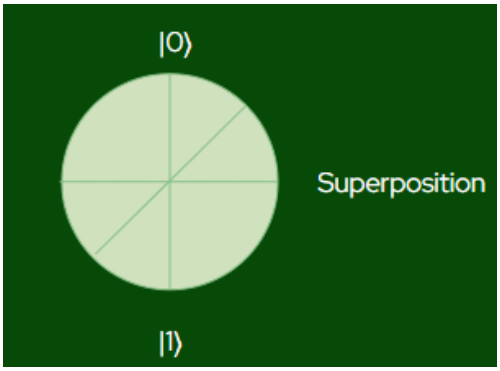


**Figure 1:** In a Bloch sphere such as the one to the right, we can see that while the qubit can be in the ground state or excited, it can also be inbetween along the x axis and be in a superposition of the two states. Over time, the state can also rotate along the equator, losing the system's coherence.

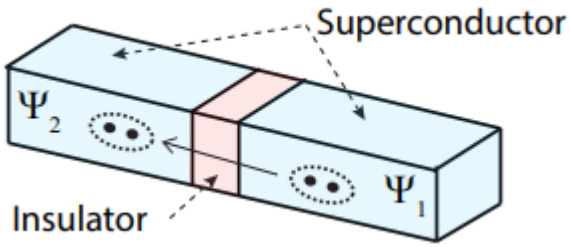


← **Figure 2**: Josephson Junctions are composed of two superconductors separated by a thin insulating layer, that Cooper pairs (shown by two dots in a dotted oval) can tunnel through, creating a current [2]. This tunneling already utilizes quantum mechanics, and the unique nonlinear characteristics of JJs make them well suited inductors for making artificial qubits.

Due to the nature of JJs and the superconductors that they are made of, they must be kept at extremely cold temperatures to function, so we put them in a Bluefer Dilation Fridge to keep them at about 4 mK when doing measurements. As the microwave signals we send in are dampened significantly by the cold, we have to use an array of amplifiers to read the output, which does introduce some extra noise to the system

a. b. c.

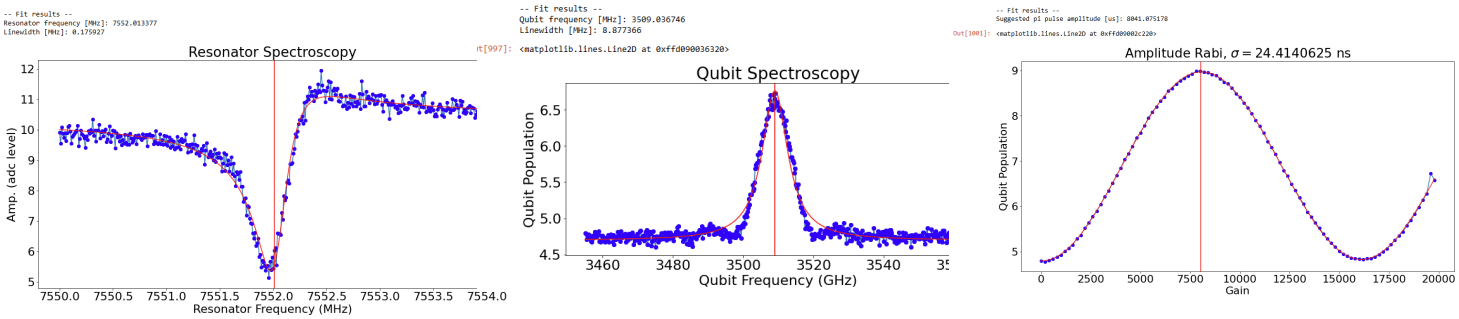


c.

d.

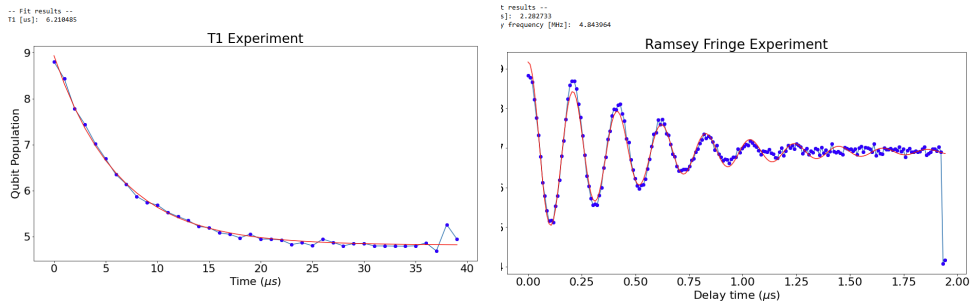


**Figure 3:** Data graphs of each characterization experiment done with Q4, 0.1 mA flux on our PURCQ circuit. c. T1 is the relaxation time. d. Ramsey Fringe Experiment is the dephasing time.

In order to actually do experiments with these quantum circuits, we first have to characterize each qubit so we know how they react to different signals, time, and noise (and negate errors). This allows us to properly optimize the system for our experiments and get accurate data. The most important of these basic characterizations are resonator and qubit frequencies, Rabi oscillations, relaxation time, and dephasing time. For all of these, we send in a microwave pulse to the system. Our signals only interact with the qubits via the resonator (aka cavity), so finding the cavity's resonant frequency for each qubit is vitally important to being able to collect data. To find the frequency of the qubit, we actually send in an additional microwave pulse to excite the qubit, giving this experiment the moniker "two tone spectroscopy". Rabi oscillations model the oscillations between excited and ground qubit states, and can tell us both the time between these states, and the amplitude of the oscillations, giving us extra parameters to plug into our code. Relaxation time tells us how long it takes a qubit to naturally go from excited to ground states, and dephasing tells us how much time passes before the qubit starts to lose coherence. All of these experiments must be done for each individual qubit in the circuit before more advanced simulations can be done. Additionally, results for each of these change with flux if the qubit is flux tunable. After learning how to take these measurements, putting a new qubit system into our fridge, and adjusting the code, I began the process of characterizing this system and laid the groundwork for further characterization and experiments with this circuit.

I would like to thank the Purdue Department of Physics and Astronomy for giving me this research opportunity and accommodating me this summer. I would also like to thank Professor Ma and everyone in his lab for the support and patience I've been given this summer as I learned all about superconducting quantum circuits. I would like to specifically thank Hebah Goderya for her daily help in coding, troubleshooting, and just teaching me everything I needed to know. Finally, this material is based upon work supported by the National Science Foundation through the Research Experience for Undergraduates program under Grant Number PHY-2244297. Without this support, this summer wouldn't have been possible for me, and I deeply appreciate it.

References:

[1] J. J. García Ripoll, *Quantum Information and Quantum Optics with Superconducting Circuits*. Cambridge, United Kingdom: Cambridge University Press, 2022.

[2] M. Naghiloo and Murch Lab, *Introduction to Experimental Quantum Measurement with Superconducting Qubits*, Apr. 2019. [Online]. Available: https://arxiv.org/pdf/1904.09291

# Kinetic Inductance Measurements of Superconducting Heterostructures

*Aidan Jacobsen*[1], *Leonid Rokhinson*[1]

[1]Purdue University, IN

Topological insulators are a class of material that has been proposed to host exotic quasiparticles such as Majorana Zero Modes when proxitized with S-wave superconductivity. These excitations lay the foundation for topological quantum computing if braiding and fusion operations can be performed with them on a 2D surface. Before attempting to manipulate these excitations, a first step is to confirm that this material exhibts the properties that are predicted by theorists. One prediction regards the structure of the superconducting gap for the surface states.

Traditional superconductors carry current with zero dissipation because the electrons pair up into "Cooper pairs" that form the ground state condensate of the superconductor. When current is applied, the whole ground state adjusts and no electrons scatter because there is a finite amount of energy required for a single electron to scatter. This finite amount of energy is known as the superconducting gap. For these S-wave superconductors, the energy required to excite a quasiparticle out of the ground state is independent on the direction that the quasiparticle would be moving.

However, theorists have predicted other types of superconductivity where the superconducting gap is anisotropic. This means that there are some directions in which exciting a quasiparticle takes zero energy. One example of a proposed material that would exibit a zero energy excitation is a 3D topological insulator's surface state that has been proximitized with S-wave superconductivity when an in-plane magnetic field is applied. My project is to probe the structure of the gap for this surface.

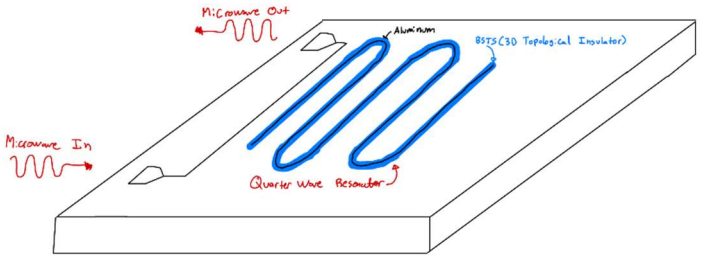


Even though cooper pairs do not dissipate power when the flow, they still take time to accelerate. This property shows up as an inductance of the superconducting wire. Specifically, the inductance due to the acceleration of Cooper pairs is known as "kinetic inductance." This property can be directly probed by constructing a quarter wave microwave resonator using BSTS (a 3D topological insulator) and aluminum and measuring how the magnetic field and temperature affect the resonant frequency of the circuit. This design is shown above.

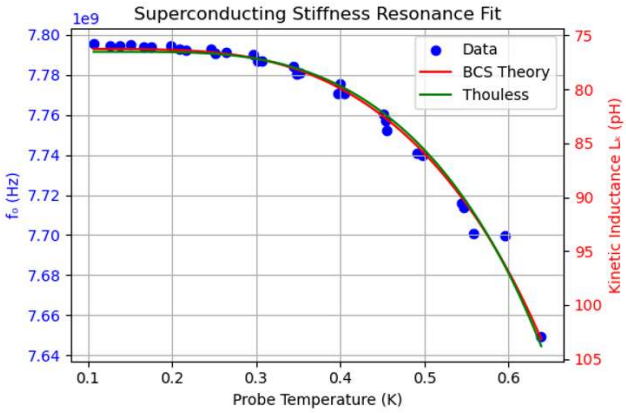


To demonstrate that our measurement setup is valid, I first measured a resonator terminated with an aluminum nanowire. The image to the left shows the relationship between temperature, the resonant frequency of the resonator, and the kinetic inductance of the nanowire. The experimental points are compared with the predictions of BCS theory for an S-wave superconductor.

To measure the properties of the superconducting surface states, a large and thin flake of BSTS must first be produced and transferred to an intrinsic silicon wafer. This is accomplished by exfoliating a small sample of BSTS, transferring some flakes to an empty wafer by softening the tape at 85°C before peeling it off of the wafer and leaving some flakes. The flakes' sizes are then confirmed via an AFM before a transfer process is attempted using 12% a PCL stamp. An image of a flake is shown in figure 3. Once flakes have been transferred, the remainder of the device fabrication process can move forward.

I would like to thank Prof. Rokhinson and Prof. Vayrynen for the many insightful conversations and explanations that I have had with them over the course of this project. I would also like to thank Jian Liao, Mingi Kim, Iakov Kogan, and Hao Li for helping me learn how to fabricate and measure devices this summer. This material is based upon work supported by the National Science Foundation through the Research Experience for Undergraduates program under Grant Number PHY-2244297.

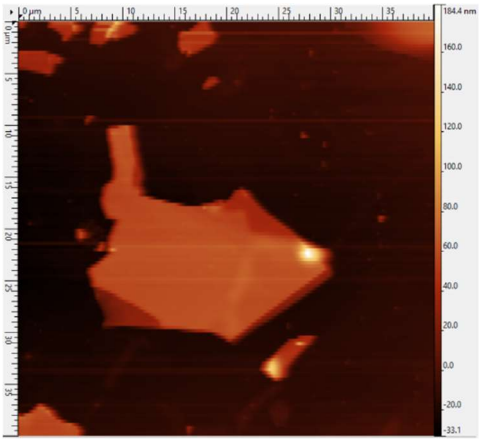

Works Cited

[1]Fu, Liang, and C. L. Kane. "Superconducting Proximity Effect and Majorana Fermions at the Surface of a Topological Insulator." *Physical Review Letters*, vol. 100, no. 9, 6 Mar. 2008, https://doi.org/10.1103/physrevlett.100.096407.

[2]Tinkham, Michael. *Introduction to Superconductivity*. Courier Corporation, 1996.

[3]Phan, D., Senior, J., A. Ghazaryan, M. Hatefipour, Strickland, W. M, Shabani, J., M. Serbyn, & Higginbotham, A. P. (2022). Detecting Induced p±ip Pairing at the Al-InAs Interface with a Quantum Microwave Circuit. Physical Review Letters, 128(10). https://doi.org/10.1103/physrevlett.128.107701

# Simulating Wave Propagation in Fractured Media

Jordan Sexton[1, 2]; Laura Pyrak-Nolte[2]

[1]*Department of Physics and Astronomy, Howard University, D.C.*

[2]*Department of Physics and Astronomy, Purdue University, IN*

Enhanced Geothermal Systems (EGS) represent the future of geothermal energy production because of its potential to harvest geothermal energy in more regions and generate electricity at greater rates than traditional geothermal systems. EGS differentiates itself from traditional systems by inducing and utilizing fractures within underground rocks to provide the necessary flow paths to transfer heat to fluids to generate electricity. The geometry and connectivity of the fractures affects heat transfer efficiency and production from EGS, which can be affected by changes in pressure and temperature. The Center for Understanding Subsurface Signals and Permeability (CUSSP) group aims to address the challenges faced when implementing EGS by developing a tool to characterize subsurface fractures and monitor their behavior over the lifetime of the reservoir.

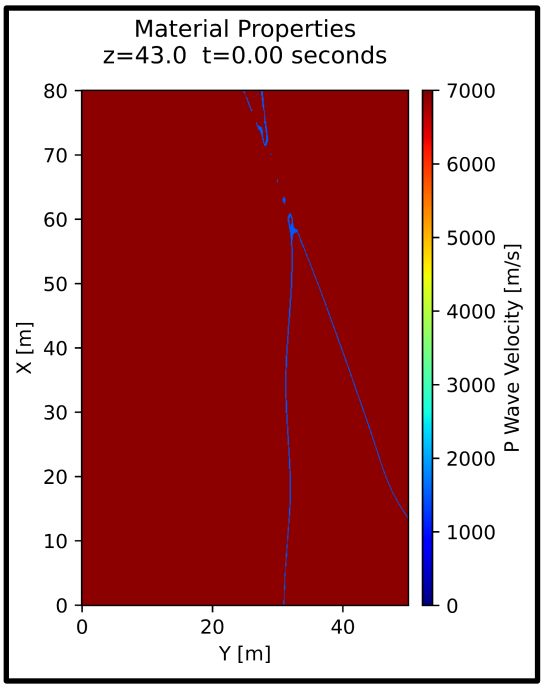


*Figure 1: 4100 ft level EGS Collab fractures at SURF plotted in SW4*

Currently, CUSSP is analyzing data from field experiments (EGS Collab) performed at the Sanford Underground Research Facility (SURF) where active seismic monitoring was performed during stimulation and shearing experiments to enhance fluid flow through the fracture system. CUSSP plans to augment their study by utilizing simulation software, such as Seismic Waves, 4th Edition (SW4), to generate synthetic seismic data for comparison with the data collected at SURF to verify the spatial distribution of fractures interpreted from the field experiments. In addition, the simulated data will enable CUSSP to predict fracture behavior based on the geometry and orientation of fractures within the system.

The purpose of this project was to explore SW4's applications within CUSSP's goals, emphasizing SW4's capabilities to represent unique fracture geometry, orientation, and conditions such as those present in the EGS Collab experiments. The undergraduate assistant for this project first developed the skills necessary to run SW4 simulations on the Negishi supercomputer at Purdue University, then gained familiarity with SW4 by testing the effects of various parameters on the simulated data, graphing simulated output, and uncovering nuances within SW4's operation. Through several material defining techniques within the software, such as the 'block' and 'ifile' command, the undergraduate displayed accurate digital representations of fracture geometry found in the field experiments at the SURF site along with other complex shapes through SW4. This project ended with the collection of preliminary simulated seismic data for future comparison with field data.

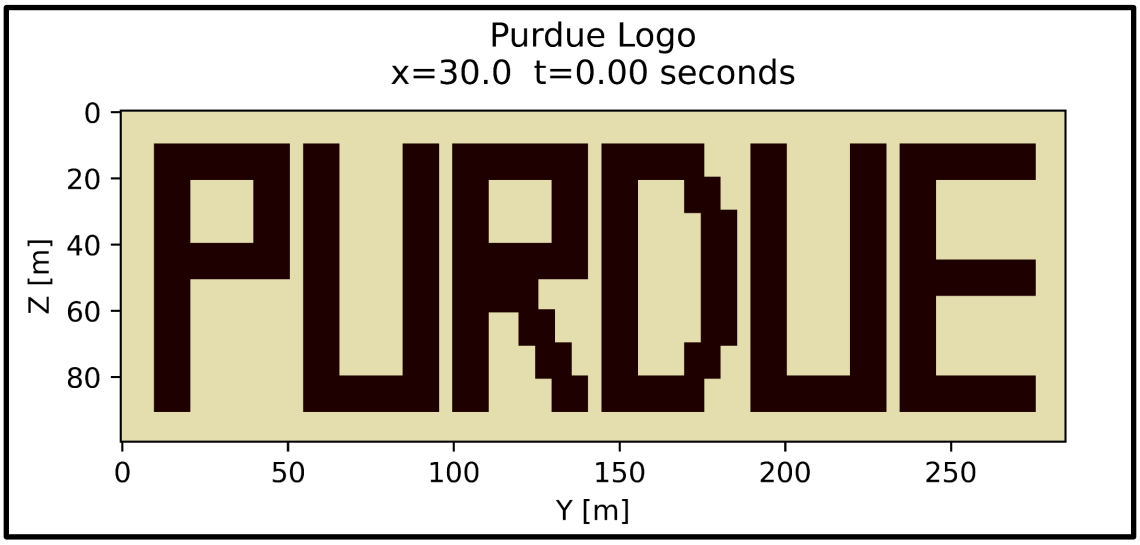


*Figure 2: 'PURDUE' plotted in SW4*

After comparing the seismic data acquired through SW4 simulations and the field data from the EGS Collab experiments, CUSSP plans to use SW4's fracture manipulation capabilities to

monitor the seismic signals of the fractures at SURF for various physical conditions, such as high and low fluid pressures, changing interface geometry, and thermal gradients.

Special thanks to Prof. Laura Pyrak-Nolte and Dr. David Nolte for providing the necessary and insightful scientific guidance regarding this project, and thank you to Alexandra Clark for her encouragement and one-on-one support throughout the duration of this research experience. Additional appreciation for the Purdue University Department of Physics and Astronomy and all of the involved faculty and staff that have supported the summer REU program.

This was supported by CUSSP (Center for Understanding Subsurface Signals and Permeability), funded by the U.S. Department of Energy (DOE), Office of Science under FWP 81834, and the National Science Foundation (NSF) REU grant PHY-2244297.

## References

Petersson, N.A. and B. Sjögreen (2017). SW4 v2.0. Computational Infrastructure of Geodynamics, Davis, CA. DOI: 10.5281/zenodo.1045297.

Petersson, N.A. and B. Sjögreen (2017). User's guide to SW4, version 2.0. Technical report LLNL-SM-741439, Lawrence Livermore National Laboratory, Livermore, CA.

Kneafsey et al. (2023). The EGS Collab – Discoveries and Lessons from an Underground Experiment Series.

# Sandstone Fracture Intersections

*David Lawrence[1], Laura Pyrak-Nolte[2]*

*[1]Culver Academies, Culver, IN [2]Purdue University, West Lafayette, IN*

Subsurface engineering applications, such as geothermal energy, environmental remediation, and the oil and gas industry, continue to grow. The US Department of Energy is expecting to grow geothermal electricity generation alone from 4 GW to 60 GW by 2050 as outlined in the *GeoVision* analysis[1]. The science and engineering knowledge must be improved to better understand and predict how reservoirs, and the rock fractures that make them up, will respond and evolve when subjected to various operations. Though current numerical tools exist, the subsurface consists of a complex web of fractures with various layers of rock and the refinement of these tools is a continuous effort. Previous work has been done on the development and characterization of sandstone single fractures[2]. The purpose of this study is to develop techniques to induce double fractures at 90 degrees from each other in sandstone and to characterize their intersection.

Unfinished sandstone core samples, cut to 19 mm diameter, were created using a masonry saw and drill press. Four notches, 1 mm wide x 1.5 mm deep, were created at 90° from each other using the xTool F1 Ultra Fiber Laser Engraver to create fracture induction sites and a single rounded groove, 3 mm wide x 2 mm deep, located at 45° between two of the notches (Fig 1) for alignment in the core holder used for x-ray analysis.

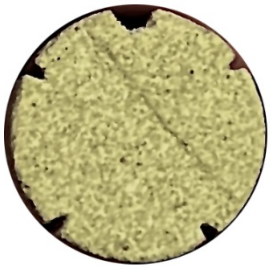

*Figure 1-Top view of sandstone core sample.*

A single fracture was induced using metal rods along opposing notches and then compressed with a vise. The sandstone core sample was examined using the Zeiss Versa 510 X-ray Microscope. Mineral fragments were included during the x-ray to use as calibration points for density (Fig 2), though only relative density was ultimately used.

*Figure 2 – Sandstone core sample within resin core holder with mineral fragments.*

A second fracture was induced using the same method and then examined using the x-ray microscpe. Preliminary analysis was conducted between the single fracture and double fracture. Segmentation of the x-ray data was conducted after each fracture using Dragonfly software based on relative density (Fig 3). Fractures were shown to form mostly along medium density regions.

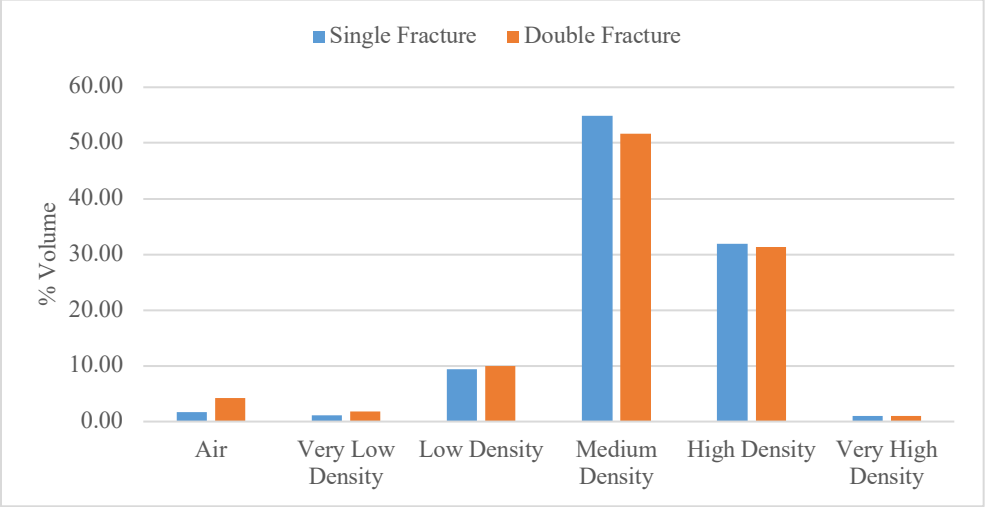


*Figure 3 – Comparison of percent volume of relative density between a single and double fracture within sandstone.*

Further analisys should be conducted using the x-ray data to further characterize the fracture and its formation.

I would like to thank Dr. Laura Pyrak-Nolte for her guidance on this research project. I would also like to thank the members of her research team, Alexandra Clark, Kyungsoo Han, Erini Christoforiduo, Ozan Altuntas, Connor Siurek, and Logan Carleton, for their immense and invaluable help with all of the training. This material is based upon work supported by the National Science Foundation through the Research Experience for Teachers program under Grant Number PHY-2244297.

**References**

[1] https://www.energy.gov/eere/geothermal/subsurface-enhancement-and-sustainability

[2] https://www.sciencedirect.com/science/article/pii/S1365160913000063

# Leveraging Online Simulations to Strengthen Specific Points in Students' Understanding in the Physics Curriculum at the Secondary Level.

*Sanjay Rebello[1], Craig Smiley[1]*

[1]Purdue University, West Lafayete, IN

This project attempts to improve certain weaknesses in physics education targeted to the top end Science, Technology, Engineering, and Math (STEM) students. Many students pursuing degrees in STEM fields take Advanced Placement (AP) courses and are evaluated at the end of the year with AP Exams. AP Physics C course is the most rigorous physics course that College Board offers, which is calculus-based, and many engineering and science universities and colleges across the country recognize that scoring well on these exams is worthy of college credit. This year over 38,000 students took the AP Physics C Mechanics Exam and over 23,000 students took the AP Physics C Electricity & Magnetism Exam. Looking at the most recent scores from the 2025 exam, areas of weakness were the following: Force & Translational Dynamics, Work & Energy, Momentum, and Rotational Dynamics on the Mechanics exam, and Electric Potential, Capacitors, Magnetic Fields, and Electromagnetic Induction on the Electricity and Magnetism exam.

The PhET Interactive Simulations project at the University of Colorado Boulder creates free interactive math and science simulations. PhET sims are based on extensive education research and engage students through an intuitive, game-like environment where students learn through exploration and discovery. There are other computer simulation resources that are also freely available for students and educators. The objective of this project is to create seven different educational activities focused on strengthening specific areas in the physics curriculum that employ these online simulations. The activities for mechanic include exploring forces and dynamics using a Rocket Sledder [1], conservation of momentum using Stacked Graph Collision [2], motion of center of mass of a system using Collision Lab [3], determining types of energy changes based up the defined system using Energy Bar Charts [4], and determining what measurements are conserved using several simulations found at A Free Particle [5]. The activities for electricity and magnetism include exploring RC, RL, LC, and RLC circuits using Circuit Construction Kit: AC – Virtual Lab. Each of these online simulation activities ask students to predict or calculate certain results based on how changes that can be produced in the simulation. Comparing their prediction and/or calculations, they are able to attain a deeper understanding of the topics at hand. Each of these activities have a follow-up multiple-choice quiz for the students to take to after completing the activity, which they may reference their activity sheets during the quiz. The purpose of the quiz is to give student quick feedback on their conclusions and their reasoning for their conclusions, and to differentiate between students who were engaged in critical thinking and those who were just copying answers from their lab mates.

Dr. Sanjay Rebello has been a sounding board for my work this summer. This work will be vetted in my classroom this year to attain feedback on the activities and the quizzes before I share them with other physics teachers on educational websites that have educational resources such as PhET, Pretty Good Physics, and Teachers Pay Teachers (for free).

This material is based upon work supported by the National Science Foundation through the Research Experience for Undergraduates program under Grant Number PHY-2244297.

References:

[1] https://www.physicsclassroom.com/interactive/newtons-laws/rocket-sledder/launch
[2] https://www.afreeparticle.com/collisions.html
[3] https://phet.colorado.edu/sims/html/collision-lab/latest/collision-lab_all.html
[4] https://www.universeandmore.com/energy
[5] https://www.afreeparticle.com
[6] https://phet.colorado.edu/en/simulations/circuit-construction-kit-ac-virtual-lab

# Investigating Ti-based metal-organic frameworks for applicability in photoelectrochemical cells.

Eva Clancy[1,2], Conor Long[3], Jenny Lockard[3], Yulia Pushkar[2]
[1] Kalamazoo College, MI, [2]Purdue University, IN, [3] Rutgers University, NJ

Metal-organic frameworks (MOF) offer promising solutions for clean energy resources due to their photoactivity and ability to catalyze water-splitting reactions (WOR). Their porous and stable crystalline structure offers a solid foundation for reactive and tunable materials to be developed and tested. MOFs can be incorporated in photoelectrochemical (PEC) cells and implemented for hydrogen fuel production. Primarily, those containing earth-abundant materials, such as Fe and Ti, hold the most interest for creating effective and economic
al green energy production.

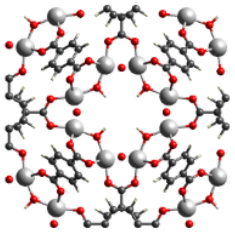

*Figure 1. MOF FeMIL125-NH2 crystal structure showing porosity and structural suitability for water splitting. [4]*

Previous research has shown promising results for Fe-based MOFs such as MIL-126 and MIL-124 [2] decorated with Ru-containing catalysts, Fe-triazolate ($Fe(ta)_2$), but combined Ti and Fe MOFs have yet to be characterized for their catalytic and photoanode properties, particularly FeMIL-125-$NH_2$. Building on the growing need for clean energy production, the characterization of MOF FeMIL-125-NH2 in a

PEC cell is achieved. In acidic and neutral environments, 24-hour chronoamperometry is taken with periodic irradiation of the photoanode to observe oxygen and hydrogen production. By investigating FeMIL125-NH2's activity, its potential as an effective photocatalyst is determined. Leading to illuminating results for FeMiL125-NH2's candidacy in the development of WOR-based clean energy resources.

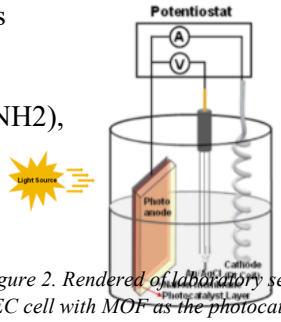


*Figure 2. Rendered of laboratory setup PEC cell with MOF as the photocatalyst layer. [1]*

The focus of my project was the characterization of this MOF (FeMiL125-NH2), which is an Fe-doped Ti-based MOF that a group at Rutgers synthesized. The Fe-doped version was of interest because of previous work that was done in Pushkar's group on $Fe(ta)_2$, which was an extremely active photoanode. Its characterization involved using chronoamperometry to obtain the highest current density possible in acidic pH 1 and natural pH 7 electrolyte. Chronoamperometry is used to measure current density as a proxy for oxygen and hydrogen production, as these are byproducts of the chemical water-splitting that occurs. Observed stability and photo reactivity of the MOF sample is probed through cyclic irradiation with visible light (60W) after 1-2 hours and 24 hours in the electrolyte bath. Data was taken using a Potentiostat and plotted/analyzed in Python.

Figure 3 shows typical chronoamperometry results I encountered while experimenting with this material. The sharp increase in current density occurs when I irradiate the sample with light, as shown in Figure 2. This is when the electrons are excited and begin conducting in the photoactive MOF. This absorbed light creates charge separation, and the charge carriers help catalyze water-splitting, releasing oxygen and hydrogen.

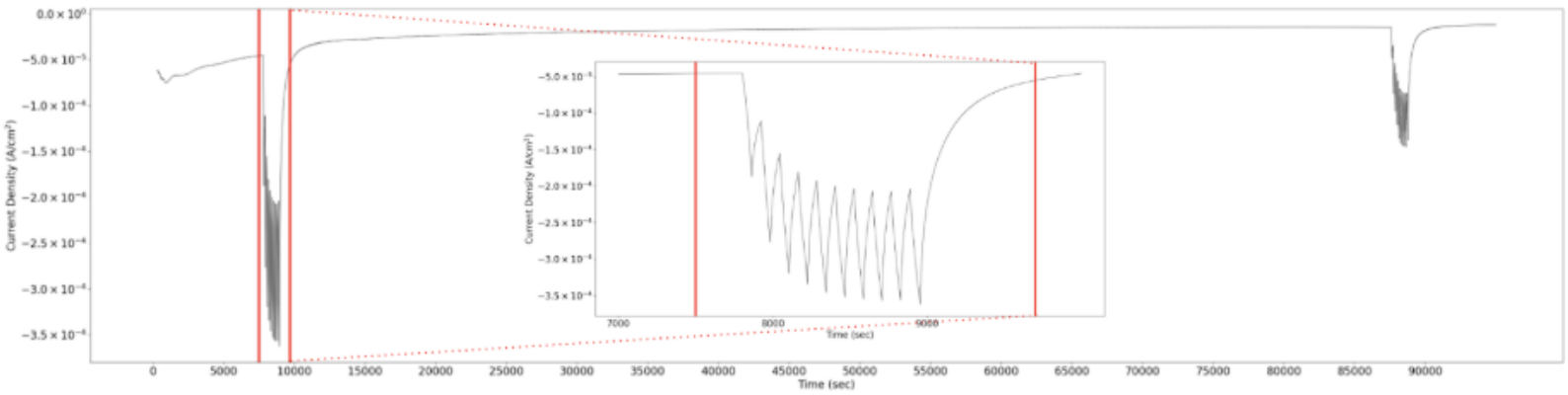


*Figure 3. 24 Hr Chronoamperometry of FeMIL125-$NH_2$ in ph1 0.1M $HNO_3$ and ph7 0.1M. 10 light/dark cycles (1 min. light/1 min. dark) applied at 2 hrs (center) and 24 hrs at a potential of +1.4V vs Ag/AgCl.*

## References

[1] Patel, J.; Purayil Dileep, N.; Bondar, V.; Gopal, P.; Anton V. Sinitskiy.; Sergei Savikhin.; Yulia Pushkar.; Fe-Triazolate Metal-Organic Frameworks (MOF) as a New Type of Water Oxidation Catalyst with Dual Photoanode Function. 2025.

[2] R. Ezhov *et al.*, Photoexcitation of Fe<sub>3</sub>O Nodes in MOF Drives Water Oxidation at pH=1 When Ru Catalyst Is Present. *Chemsuschem*, (2023).

[3] Xie, Y.; Khoo, K. S.; Chew, K. W.; Devadas, V. V.; Phang, S. J.; Lim, H. R.; Rajendran, S.; Show, P. L. Advancement of Renewable Energy Technologies via Artificial and Microalgae Photosynthesis. *Bioresource Technology* 2022, *363*, 127830.

[4] Long, Conor.; Zhang, Xiaoyi.; Lockard, Jenny V.; Pushing the heterometal doping limit while preserving long-lived charge separation in a Ti-based MOF photocatalyst. *J. Chem. Phys.* 21 November 2023; 159 (19): 194704.

[5] 22. S. Y. Lin et al., Electrochemical Water Oxidation by a Catalyst-Modified Metal-Organic Framework Thin Film. Chemsuschem 10, 514-522 (2017).

[6] 24. R. Ezhov, A. K. Ravari, A. Page, Y. Pushkar, Water Oxidation Catalyst cis- Ru(bpy)(5,5 '-dcbpy)(H2O)(2) (2+) and Its Stabilization in Metal-Organic Framework. Acs Catalysis 10, 5299-5308 (2020).

## Acknowledgements

Thank you to all collaborators and Yulia Pushkar for advising on this work.
This research is based upon work supported by the National Science Foundation through the Research Experience for Undergraduates program under Grant Number PHY-2244297.

# Expanding Twistronics to Wafer Scale 2D films

Sagarika Menon[1,2], Kyung Jun Lee[1], Priya Mishra[1], Manaswini Singh[1], Tiancong Zhu[1,3,4]

[1] Department of Physics and Astronomy, Purdue University, West Lafayette, IN, 47907

[2] School of Physics, Georgia Institute of Technology, Atlanta, GA, 30332

[3] Birck Nanotechnology Center, Purdue University, West Lafayette, IN, 47907

[4] Purdue Quantum Science and Engineering Institute, West Lafayette, IN, 47907

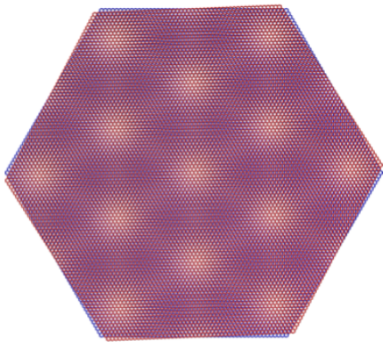

**Figure 1:** This image shows two monolayer graphene lattices stacked with the magic angle of 1.1 degrees between them. The Moire superlattice that arises as a result of this stack is consequently visible. Reproduced from [4]

First proposed in theory and then launched as an exciting new field with the experimental discovery of gate-tunable correlated insulating states and superconductivity in "Magic Angle" Twisted Bilayer Graphene (MATBG) (figure 1), twistronics examines the impact of a twist angle between the lattice interfaces of stacked 2D materials on the electronic properties of the resulting structure[1]. With applications ranging from superconducting electronics and quantum computing[2] to neuromorphic computing[3], MATBG shows significant promise as a versatile and groundbreaking material.

Most monolayer graphene samples so far have been created using a process known as scotch-tape exfoliation, as shown in figure 2. MATBG fabricated with scotch-tape exfoliated 2D materials, yielding samples limited to only a few tens of micrometers in size. Applications like the previously mentioned superconducting electronics and neuromorphic computing rely on large areas of MATBG with a uniform twist angle to produce components with consistent performance[2, 3]. This is incompatible with the scotch-tape-exfoliation method. However, Molecular Beam Epitaxy (MBE), a method of thin-film deposition that relies on , can produce high-quality thin films at the wafer scale. MBE offers a promising route to advance both fundamental studies and practical applications for twistronics in a scalable fashion. Unlike with scotch-tape-exfoliated flakes, however, it is challenging to manipulate and stack those MBE-grown thin films since they are firmly attached to the substrate on which they were grown. Ideally, we could combine the large area consistent films of MBE-grown films with the ease of manipulation of scotch-tape-exfoliated flakes. To achieve this, we need a method to

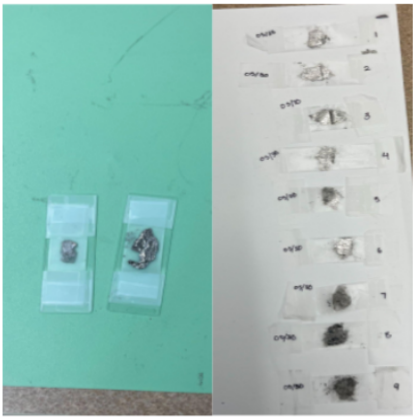

**Figure 2: (a)** Two bulk graphite mother tapes used in scotch tape exfoliation. Note that the mother tape on the left has been peeled down much thinner compared to the one on the right. **(b)** An image showing several tapes exfoliated from the mother tapes on the left with graphene flakes visible in the center.

reproducibly separate MBE films from the substrate without introducing tears or other imperfections, to use them for twistronics.

A manual procedure to perform a dry-transfer of MBE-grown materials onto a desired substrate was demonstrated by a team at Ohio State University[5]. This process starts by spin coating the substrate with our MBE film on it in (PCL). Then they attach a (PDMS) stamp with thermal release tape onto the spin-coated substrate. Then using a roller we slowly peel the film and everything on top of it off of the substrate. The PDMS stamp acts to cushion the film and reduces tearing. The roller leads to a smaller angle between the substrate and film during the peel off, making it much less likely to find tearing and wrinkles.

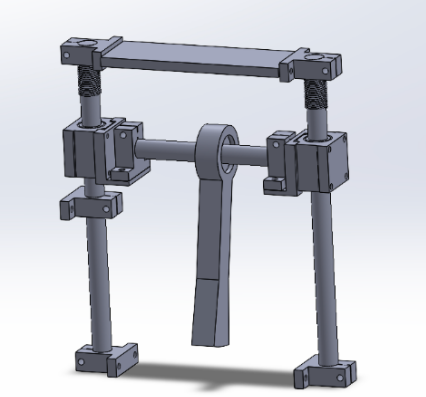

**Figure 3:** This figure shows a Computer-Aided Design (CAD) model of one of our designs. The stepper motor rail used to carry the sample is not shown here but in our final design, is bolted to the bottom supports and is what the roller piece rests on.

We endeavor to build upon this procedure, creating a motorized machine that performs this process in a more consistent and reproducible manner. Our device (figure 3) is designed to handle the roller process, which, in the Ohio State procedure, is the most susceptible to variation when done manually. We want our machine to allow for easy sample loading, adjustable pressure applied to the sample during rolling, slow movement for gentle release, and we want to mimic both the translational and rotational movement of the roller across the sample surface. With this approach, we will be able to integrate MBE-grown materials into twistronics research and study the electronic properties of these structures at the wafer scale, compare these results with twistronics samples produced with scotch-tape-exfoliated flakes (also fabricated over the course of this project), and bridge the gap between discoveries in fundamental science and scalable device applications.

I would like to thank Dr. Tiancong Zhu for all his guidance and help over the course of this project, Kyung Jun Lee, Priya Mishra, and Manaswini Singh for teaching me how to exfoliate and stack 2D materials, and Christopher Ulate and Brayden E. Kauffmann for helping me put together the final machine. This material is based upon work supported by the National Science

Foundation through the Research Experience for Undergraduates program under Grant Number PHY-2244297.

**Works Cited**

[1]Andrei, E. Y., & MacDonald, A. H. (2020). Graphene bilayers with a twist. *Nature Materials*, *19*(12), 1265–1275. https://doi.org/10.1038/s41563-020-00840-0

[2] Wang, J., Mu, X., Wang, L., & Sun, M. (2019). Properties and applications of new superlattice: twisted bilayer graphene. *Materials Today Physics*, *9*, 100099–100099. https://doi.org/10.1016/j.mtphys.2019.100099

[3] Chen, M., Xie, Y., Cheng, B., Yang, Z., Li, X.-Z., Chen, F., Li, Q., Xie, J., Watanabe, K., Taniguchi, T., He, W.-Y., Wu, M., Liang, S.-J., & Miao, F. (2024). Selective and quasi-continuous switching of ferroelectric Chern insulator devices for neuromorphic computing. *Nature Nanotechnology*, *19*(7), 962–969. https://doi.org/10.1038/s41565-024-01698-y

[4] Sato, K., Hayashi, N., Ito, T., Masago, N., Takamura, M., Morimoto, M., Maekawa, T., Lee, D., Qiao, K., Kim, J., Nakagahara, K., Wakabayashi, K., Hibino, H., & Norimatsu, W. (2021). Observation of a flat band and bandgap in millimeter-scale twisted bilayer graphene. *Communications Materials*, *2*(1), 1–6. https://doi.org/10.1038/s43246-021-00221-3

[5] Li, Z., Zhou, W., Swann, M. T., Vika Vorona, Scott, H. E., & Kawakami, R. K. (2025). Full-film dry transfer of MBE-grown van der Waals materials. *2D Materials*, *12*. https://doi.org/10.1088/2053-1583/adc611

# Development of a Photon Counting System and Co-Sublimation Chamber for DBT-Doped Anthracene Crystal Growth

**Patrick Bak**[1], **Jonathan Hood**[2]
[1]Ohio Northern University, Ada, OH; [2]Purdue University, West Lafayette, IN

Single-photon emitters (SPEs) are light sources that release one photon at a time, a requirement for many experiments and technologies in quantum optics. They are essential for secure quantum communication, optical quantum computing, and high-resolution sensing, where precise control over individual photons is critical. One promising SPE system uses dibenzoterrylene (DBT) molecules embedded in anthracene (Ac) crystals. This approach stands out due to its excellent photostability, narrow zero-phonon line [1,2]. Recent research has shown that DBT-based emitters can be coupled to waveguides and cavities, making them viable for use in complex quantum photonic circuits [3].

However, scalable adoption is limited by the lack of standardized, reproducible synthesis techniques and accessible tools for locating and characterizing individual emitters. This REU project addressed these challenges through the development of two complementary technologies: (1) a cost-effective, open-source photon counting system based on an ESP32 microcontroller, and (2) a custom-built co-sublimation vacuum chamber for controlled growth of DBT-doped anthracene crystals. Together, these tools aim to lower the barrier to entry for SPE research and improve emitter reproducibility and integration across quantum optics platforms.

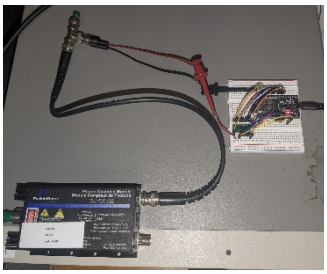

*Figure 2: Photon Counting Setup, Bottom left is APD, right is ESP32 and 12-bit counter*

The photon counting system is built around an ESP32 microcontroller and a 12-bit SN74LV4040 binary counter. PerkinElmer SPCM-AQRH-13-FC, a silicon avalanche photodiode (APD)–based single-photon counting module (hereafter, APD) produces a 2.2 V pulse upon detecting a photon. It is connected via a BNC cable to a 50 Ω resistor for impedance matching (top left of Figure 1); the black lead is grounded, while the red lead connects to the CLK pin of the counter. Powered by the ESP32's 3.3 V output, the counter provides a binary output from QA to QL. Every 10 ms, the ESP32 reads the current binary state and calculates the difference from the previous value, transmitting the result to a computer. This low-cost system was compared against the commercial Stanford Research Systems SR400 photon counter, demonstrating notable advantages in affordability, programmability, and compactness. Because the ESP32 is programmed using Python, the system is highly customizable and easy to adapt for specific experimental needs. While the SR400 offers superior timing precision and supports count rates up to ~200 MHz, the ESP32-based system is limited by its 10 ms sampling window, a maximum count rate of ~400,000 counts per second, and timing resolution constrained by interrupt latency and CPU overhead. As such, it is not suitable for applications requiring accuracy better than 1%. Despite these limitations, the ESP32 system

produced count-rate measurements consistent with the SR400, making it a reliable and cost-effective alternative for applications where ultra-high-speed precision is not essential.

*Figure 2: New Custom Vacuumed Chamber*

For crystal growth, a custom vacuum chamber (shown in Figure 2) was constructed using standard DERNORD 4" stainless steel Tri-Clamp fittings, including a transparent inline sight glass for monitoring and various reducers to interface with sensors and valves. A DERNORD dual ¼" NPT adapter at the top of the chamber allowed for connection to a vacuum pump and nitrogen line via needle valves, compression fittings, and a Y-adapter. A vacuum gauge was mounted to monitor internal pressure. The lower section of the chamber included a DERNORD 4" to 1.5" Tri-Clamp reducer to a DERNORD 100mm thermowell that housed a K-type thermocouple and a 24 V, 70 W cartridge heater for temperature control from a BERM-series PID temperature controller. On top of the thermowell sat a machined copper holder to hold a glass crucible. Anthracene (Ac) powder mixed with DBT is placed in a glass crucible, which is kept at 550 mbar in a static nitrogen environment. Sublimation occurs at around 255 °C, where the Ac crystalizes in the N2 and falls on PVC. This method is inspired by previously reported strategies for embedding single DBT molecules in crystalline organic matrices to generate photostable, narrowband emitters suitable for quantum optics [1,2]. Preliminary trials successfully produced pure anthracene crystals (No DBT), characterized by microscopy as small, plate-like crystals exhibiting birefringent properties indicative of high crystallinity and purity. A representative microscope image (Figure 3) shows a diverse distribution of crystalline morphologies, including hexagonal and needle-like structures, showing the presence of well-ordered anthracene crystals. The variation in size and shape suggests non-uniform cooling or deposition rates, which may be addressed through future refinements. The intended growth of DBT-doped anthracene crystals remains incomplete. Future improvements include implementing a delayed cap-removal method to ensure sublimation happens at 255 °C and not before, and stacking PVC plates for crystal stratification based on crystal size or density to improve selective deposition quality. These refinements aim to enhance emitter quality and integration

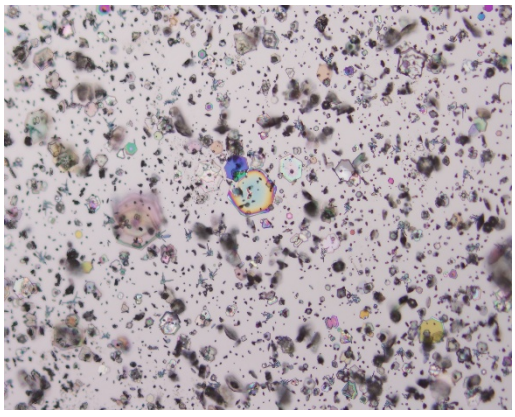

*Figure 3: Ac Crystals Grown in Custom Chamber*

with photonic structures, as outlined in recent work from the Hood Lab group at Purdue University [3].

A preliminary integration of the photon counter and co-sublimation chamber involved scanning anthracene crystals using an optical setup equipped with automated spatial control. This proof-of-concept produced two-dimensional fluorescence intensity maps (Figure 4), illustrating the ability to resolve spatial emission distributions within the crystal—an essential step for identifying DBT emitter locations once successful doping is achieved [3].

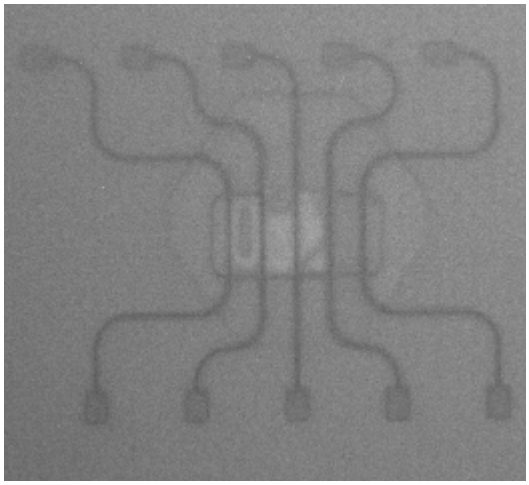

*Figure 4: Picture of Photonic Integration*

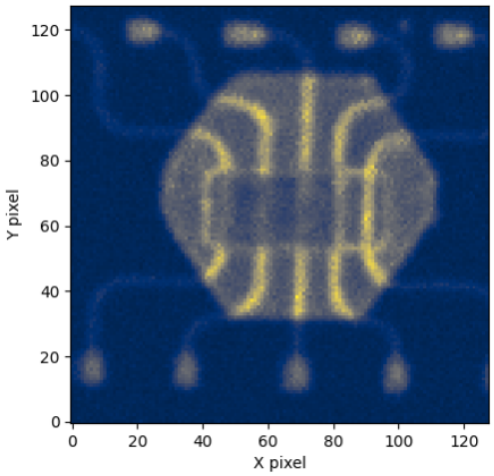


*Figure 5: Scan of Photonic Integration*

The chip sample used in this scan was fabricated and provided by Christian Lange. Figure 5 shows a representative fluorescence map of the photonic integration where the hexagon is the anthracene crystals doped with DBT, where brighter regions correspond to higher photon emission intensities.

Overall, the two main summer projects—building a low-cost photon counting system and creating a custom co-sublimation chamber—provided important tools for future work in quantum photonics and organic crystal growth. These projects show that it's possible to copy key functions of expensive commercial equipment using affordable, customizable alternatives. This opens the door for more labs and students to take part in single-photon emitter research. With further improvements, the system could be expanded to include automatic emitter detection, better spectral filtering, and real-time feedback during crystal growth or scanning. The next steps will focus on successfully adding DBT to the crystals, making the crystal growth process more consistent, and scaling the setup for scanning more samples or integrating with photonic chips. These upgrades will help move the project closer to creating reliable, high-quality single-photon sources for use in future quantum technologies

*This material is based upon work supported by the National Science Foundation through the Research Experience for Undergraduates program under Grant Number PHY-2244297.*

**References:**

[1] Penglong Ren et al., *Nature Communications* **13**, 3982 (2022). DOI: 10.1038/s41467-022-31603-x.

[2] Shangming Wei et al., *Physical Review Applied* **13**, 064023 (2020). DOI: 10.1103/PhysRevApplied.13.064023.

[3] Christian M. Lange et al., "Cavity QED with molecular defects coupled to a photonic crystal cavity," arXiv preprint arXiv:2506.01917 (2025).

# Graphene and hBN Encapsulation of 2D FeTeSe for Superconducting Proximity Studies

*Madeleine Spark[1,2], Andres Eduardo Llacsahuanga Allcca[2], Yong P. Chen[2]*
[1]Colorado College, Colorado Springs, CO, [2]Purdue, West Lafayette, IN

Two-dimensional (2D) superconductors offer a rich platform for exploring exotic electronic phenomena, yet their electrical properties remain largely unexplored due to fabrication challenges. In this project, we develop ways to investigate the 2D limit of iron telluride selenide (written $Fe(Te_{1-x}Se_x)$, Fe(Te,Se), or simply FTS), an iron-based superconductor and topological superconductor candidate [1]. Thin-film (~50nm) FTS has been shown to superconduct [2], but more evidence is needed to determine the superconductivity of ultra thin-film (.6-5 or few layer) FTS. To isolate ultra-thin films of FTS we used gold-template-assisted mechanical exfoliation [3], and FTS flake thickness on the nanometer scale was confirmed using AFM.

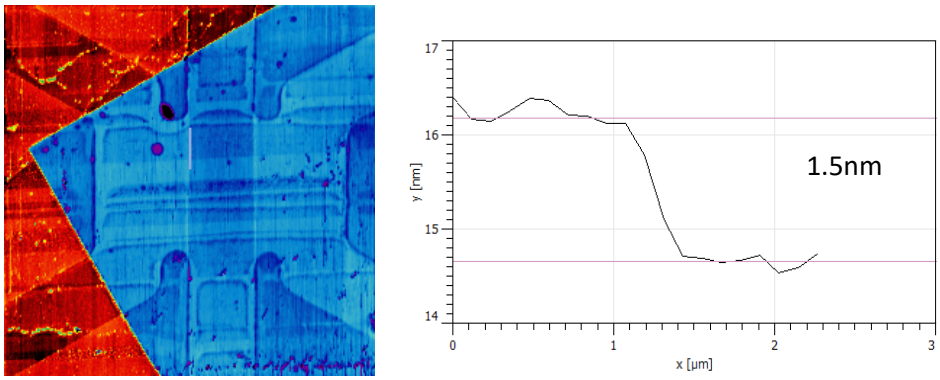


***Figure 3*** *(Left) AFM image of FTS flakes exfoliated onto gold and silicon-patterned wafer. Capped with graphene and hBN. (Right) Vertical variation of the sample's surface along the pink line marked on the left image. 1.5nm drop suggests this is the thickness of our FTS flakes. Note that contaminants trapped between the FTS and graphene/hBN layers are a possible source of error.*

Due to the air sensitivity and instability of FTS in its thin-film form as well as limitations in size and scale of its yield, we developed van der Waals heterostructures that cap the FeTeSe with a layer of graphene and a protective layer of hexagonal boron nitride (hBN). To achieve this, we test multiple dry transfer methods. These included stamps made of a combination of polydimethylsiloxane (PDMS) and either polycarbonate (PC) or polypropylene carbonate (PPC) films. Raman spectra of FTS flakes after annealing at 180 °C show changed chemical compositions similar to FTS flakes exposed to air for extensive periods of time, suggesting degradation of FTS due to heat. Therefore, we focused on minimizing thermal exposure during the transfer process to preserve the integrity of the FeTeSe layer. PPC's lower glass transition temperature ($T_g$) allows for transfers at lower temperatures. 'Pick-up' with PPC can be done at approximately 40 °C while 120 °C is needed for PC; 'drop-down' with PPC can be done at temperatures as low as 70 °C while 180 °C is needed for PC [4].

These heterostructures will allow us to probe potential superconducting proximity effects in graphene at temperatures below the critical temperature of FTS. Due to its 2D nature and proximity, changes in resistivity of the graphene may reveal electrical and ferromagnetic properties of FTS, giving us a way to bypass measuring FTS directly. The method of exfoliating FTS directly onto pre-

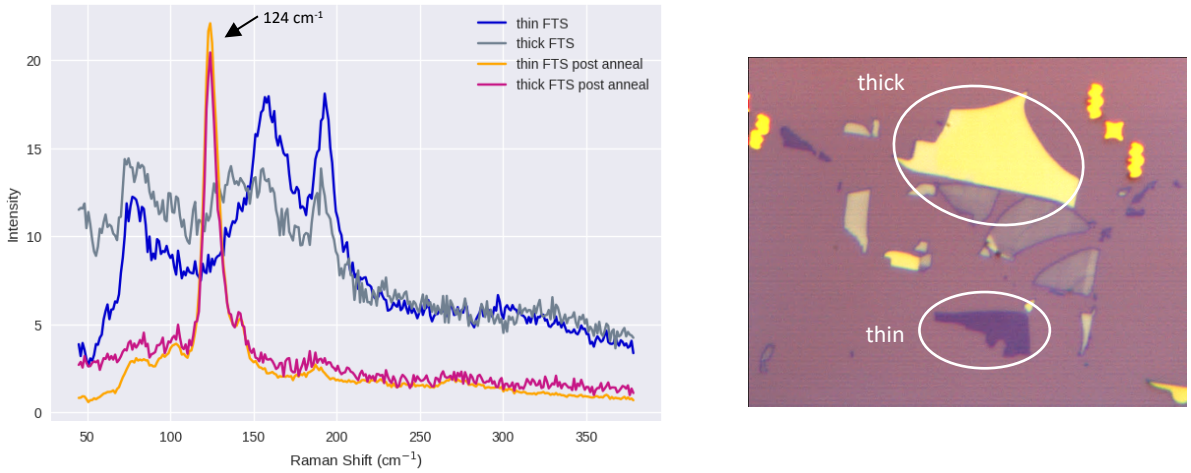


***Figure 4*** *(Left) Raman spectra of two FTS flakes on $SiO_2$ before and after annealing at 180 °C for approximately ten minutes to mimic the drop-down portion of PC film-assisted transfer. The peak at 124 $nm^{-1}$ appears only after annealing, suggesting degradation. It likely corresponds with a vibrational mode involving heavier atoms like the tellurium or selenium and could indicate aggregation of one of those two. (Right) Optical image of the thin and thick FTS flakes.*

patterned $Au/SiO_2$ wafers designed so that the gold can act as contacts also bypasses the need for etching or lithography after exfoliation, which the FTS flakes would likely not survive. This method,

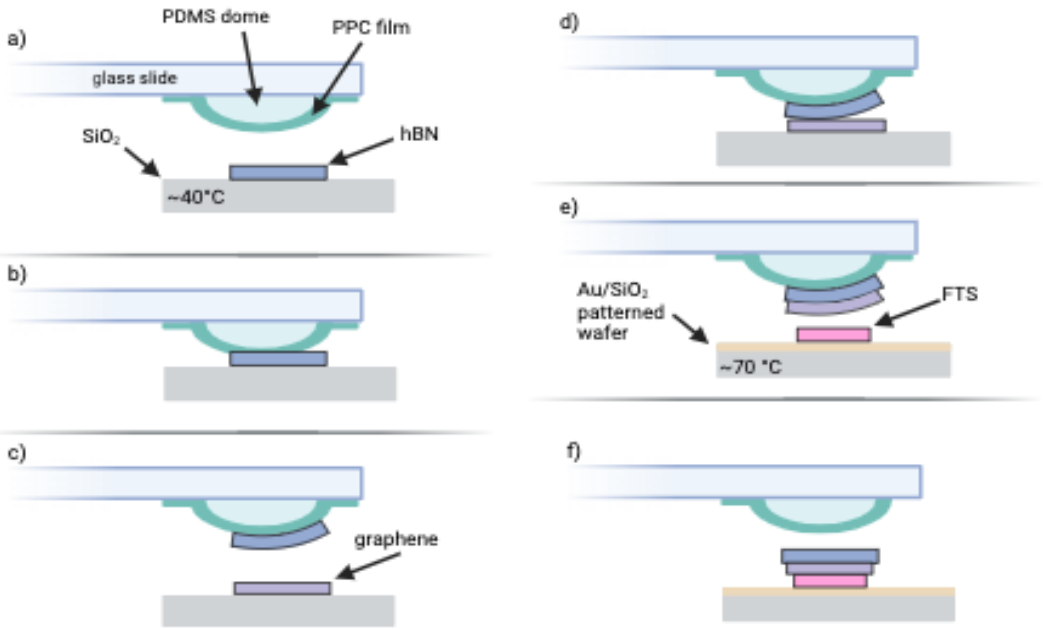


***Figure 5*** *Schematic of the dry transfer process using PDMS and PPC to pick up graphene/hBN from $SiO_2$ then drop onto FTS.*

however, introduces risks of shorting across contacts by peripheral flakes from the exfoliation or transfer steps. We easily deal with these by etching around the contacts with an AFM tip. Figures 4 and 5 show the results of our control measurements and will be important in identifying proximity effects in the completed devices. Although completed FTS/graphene/hBN devices of sufficient quality remain in the future along with their measurements, we now have preliminary data and clearer methods which will make future work more meaningful and efficient. Continuing this work, we hope to not only understand better the 2D form of this promising material for applications in quantum

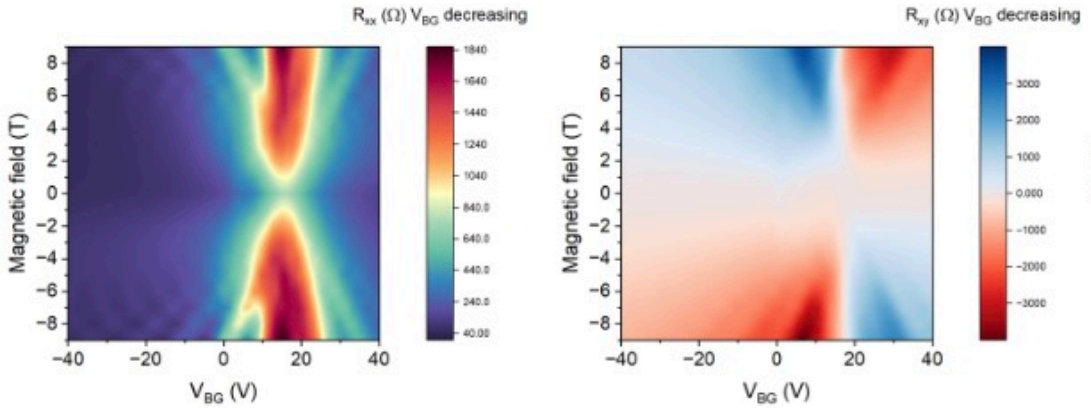


***Figure 6*** *Magneto-transport measurements. (Left) Longitudinal resistance as a function of magnetic field and back gate voltage. The Landau fan is evidence of the quantum hall effect. (Right) Hall resistance as a function of magnetic field and back gate voltage.*

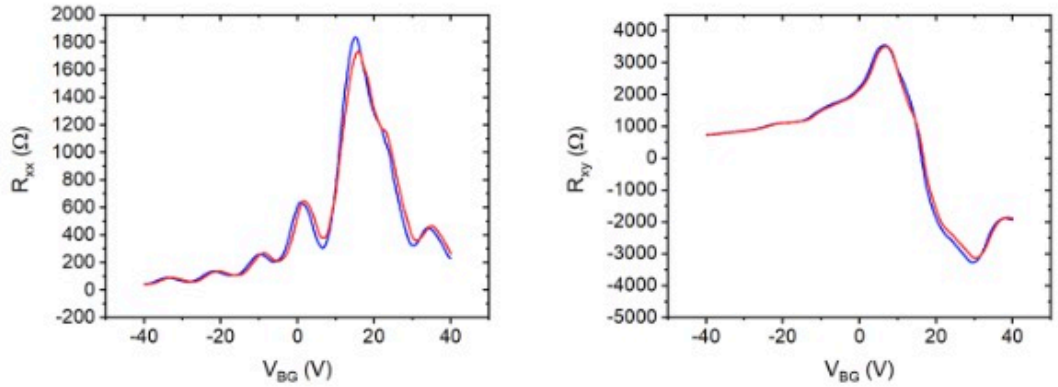


***Figure 7*** *Longitudinal and Hall resistances across magnetic field sweeps back and forth show no hysteresis or direction dependence.*

computing and electronics in general, but also to establish a reliable platform for measuring the electronic properties of fragile 2D superconductors and exploring their interactions with adjacent materials.

I would like to express my gratitude for post doctorate Andres Allcca for his kindness and patience this summer and for his exceptional generosity in sharing and giving thoughts, knowledge, experiences, and guidance. I would also like to thank post doctorate Nithin Abraham for his very thoughtful explanations, especially of excitons and the photoluminescence measurement setup. A special thanks to PhD student Akshay Agrawal for sharing his valuable knowledge and advice and helping me feel welcome in the lab. Finally, I would like to thank Prof. Chen for welcoming me into his group, leading a community that allowed me to learn from many people, and giving me feedback. A huge thank you as well to the Department of Physics and Astronomy at Purdue, including everyone who made this experience smoother and more fun.

This material is based upon work supported by the National Science Foundation through the Research Experience for Undergraduates program under Grant Number PHY-2244297.

## References


[1] Qiu, G., Yang, HY., Hu, L. *et al.* Emergent ferromagnetism with superconductivity in Fe(Te,Se) van der Waals Josephson junctions. *Nat Commun* **14**, 6691 (2023). https://doi.org/10.1038/s41467-023-42447-4

[2] Zhuang, J., Yeoh, W., Cui, X. *et al.* Unabridged phase diagram for single-phased $FeSe_xTe_{1-x}$ thin films. *Sci Rep* **4**, 7273 (2014). https://doi.org/10.1038/srep07273

[3] K. Wu, H. Wang, M. Yang, L. Liu, Z. Sun, G. Hu, Y. Song, X. Han, J. Guo, K. Wu, B. Feng, C. Shen, Y. Huang, Y. Shi, Z. Cheng, H. Yang, L. Bao, S. T. Pantelides, H.-J. Gao, Gold-Template-Assisted Mechanical Exfoliation of Large-Area 2D Layers Enables Efficient and Precise Construction of Moiré Superlattices. *Adv. Mater.* 2024, 36, 2313511. **https://doi.org/10.1002/adma.202313511**

[4] Kinoshita, K., Moriya, R., Onodera, M. *et al.* Dry release transfer of graphene and few-layer h-BN by utilizing thermoplasticity of polypropylene carbonate. *npj 2D Mater Appl* **3**, 22 (2019). https://doi.org/10.1038/s41699-019-0104-8

# Analyzing Remains of Dramatic Stellar Death

Zachary Pleska[1], Noah Zimmer[2], Danny Milisavljevic[2]

[1]Lycoming College, Department of Physics and Astronomy, 1 College Place, Williamsport, PA, 17701, USA

[2]Purdue University, Department of Physics and Astronomy, 525 Northwestern Avenue, West Lafayette, IN, 47907, USA

## 1. Isolating Supernova Remnant G292 utilizing PSF Photometry

G292 is a core collapse supernova remnant approximately 6kpc away in the Centaurus constellation (more science about these supernovae below) [1]. This project utilizes optical to near-IR imaging from the Magellan Telescopes in Chile, focusing most strongly on the OIII doublet at 4959 and 5007 angstroms. Two narrow-band images are taken with the telescope: an on-band image that captures the OIII line feature, and an off-band image that aims to capture the background continuum emission.

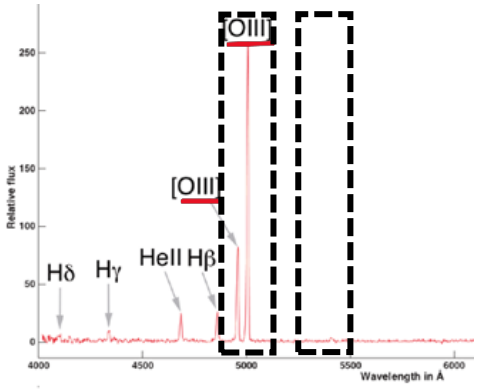


Figure 1: A line emission spectrum displaying the OIII emission doublet [2]. The boxes display approximate wavelength ranges for both on-band (left) and off-band (right) images.

Our goal is to isolate the OIII remnant emission, which requires a proper background star subtraction. We first align the on-band and off-band images and reproject the images to the same shape. The images must be dimensionally exact for proper alignment and subtraction. From here, we mark the locations of all the unwanted stars that exist in the off-band image. However, because these two observations were taken on separate filters, a direct star subtraction is not suitable, as the 'point spread function' (PSF) of each filter is different, or the star's flux dissipates differently from its peak point. This is where PSF photometry can be applied.

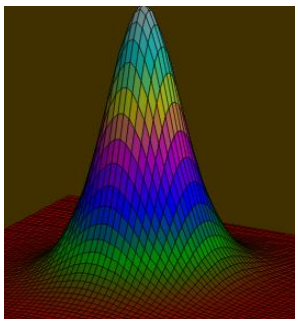

Figure 2: A visual example of a mathematical Gaussian model used in PSF photometry.

From the located stars in the off-band, this catalog can be sorted through in the on-band image to select ideal and varying candidates to apply our PSF model. This PSF model will be able to calculate the contained flux and how that flux changes radially. Knowing the peak pixels of all the sources from our star finder and applying PSF photometry from our fitted models will allow us to properly remove the stars from the on-band image, leaving the OIII emission standing alone. Along with the normal stars, there are also

other contaminants in the image, including saturated stars (stars with too much observed flux that overflow their pixel bins), over-subtracted backgrounds, and other detector defects during observation. Isolating the OIII emission is very useful for analyzing the morphology of the remnant, which encodes information about the explosion dynamics and subsequent interaction with surrounding gas.

## 2. A Model for Extragalactic Supernovae Candidates Utilizing Spectral Decomposition and Principal Component Analysis

Core collapse supernovae (CCSN) are energetic explosions initiated by the gravitational collapse of a massive star core. These events produce heavy elements and dust that provide the foundation for new stars and planets, making them crucial for the evolution of galaxies. Investigating the nucleosynthetic yields of these explosions and the physical characteristics of the produced dust grains (size, composition, distribution) improves our understanding of CCSN explosion dynamics [3,4,5,6]. However, because CCSN are not abundant in the Milky Way Galaxy, the number of observations with high resolution is limited, becoming a leading factor for the poor dust and elemental constraints using current models. We present an analysis of high-resolution images of the supernova remnant Cassiopeia (Cas) A made by the James Webb Space Telescope that attempts to address this uncertainty.

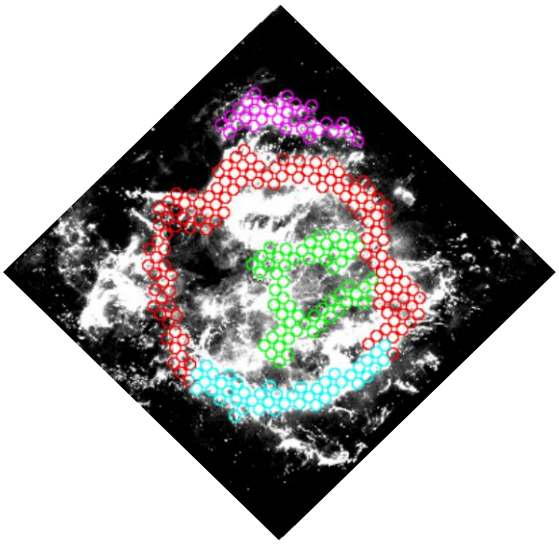

Figure 1: Regions associated with Cas A:

Full Shell – Partial Shell – Circumstellar Medium – Green Monster

Using images obtained with the NIRCam and MIRI instruments, we measure the spectral energy distribution (SED) of gas and dust between 5 and 25 microns and attempt to identify the dominant components of emission. We started by identifying 4 regions of interest, shown in Figure 1: A partial shell of metal-rich reverse-shock ejecta, the full shell of metal-rich reverse-shock ejecta, the circumstellar material surrounding the star prior to explosion, and the characteristic Green Monster in the center of the remnant [7,8]. The Green Monster and the CSM are composed of gas released by the star prior to going supernova, enhanced in helium and nitrogen. The full and partial shells are mostly composed of ejecta from the explosion itself, rich in sulfur, oxygen, argon, and neon. An

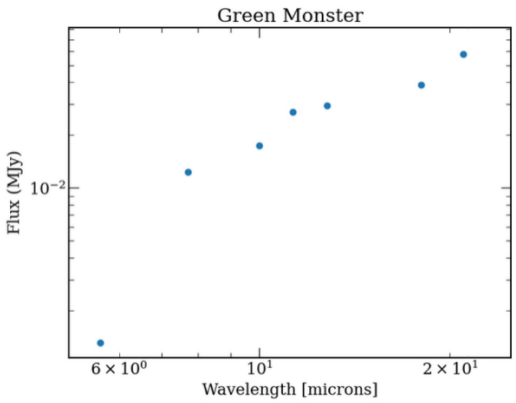


Figure 2: Total spectral energy distribution for regions in the Green Monster

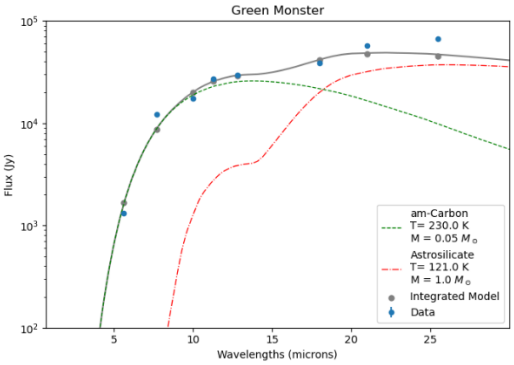


Figure 3: Fitted dust model components for the Green Monster

example of this SED for the Green Monster is shown in Figure 2. It describes the flux captured in those regions per wavelength bin, with a total of 7 wide-band filters.

After capturing the SEDs of these regions, we aim to model these dominant emission features in order to make estimates about dust properties and correlations between the dust and chemical abundances of the supernova ejecta. An example of this dust model can be found in Figure 3 for the Green Monster. This model with a two-component fit tells us that the dominant components in the Green Monster are amorphous carbon and astrosilicate.

Note, examples shown here are subregions, focusing on specific morphology and their dominating components. Moving forward, I would like to see this work applied across the entire remnant using more regions. And to use principal component analysis (PCA) to identify additional contributions to the overall emission. Furthermore, this work on the resolved supernova debris field can inform analyses about unresolved extragalactic supernovae.

## References

[1]Temim, T., Slane, P., & Raymond, J. C., et. al. (2022). Snr G292.0+1.8: A remnant of a low-mass-progenitor stripped-envelope supernova. *The Astrophysical Journal*, *932*(1), 26. https://doi.org/10.3847/1538-4357/ac6bf4.

[2]Garde, O. (n.d.). *Planetary nebulae confirmation*. Shelyak Instruments. https://www.shelyak.com/planetary-nebulae-confirmation/?lang=en.

[3]Arendt, R. G., Dwek, E., & Kober, G., et. al. (2014). Interstellar and ejecta dust in the Cas A supernova remnant. *The Astrophysical Journal*, *786*(1), 55. https://doi.org/10.1088/0004-637x/786/1/55.

[4]De Looze, I., Barlow, M. J., & Swinyard, B. M., et. al. (2016). The dust mass in Cassiopeia A from a spatially resolved *Herschel* analysis. *Monthly Notices of the Royal Astronomical Society*, *465*(3), 3309–3342. https://doi.org/10.1093/mnras/stw2837.

[5]DeLaney, T., Rudnick, L., & Stage, M. D., et. al. (2010). The three-dimensional structure of Cassiopeia A. *The Astrophysical Journal*, *725*(2), 2038–2058. https://doi.org/10.1088/0004-637x/725/2/2038.

[6]Hwang, U., & Laming, J. M. (2012). A *Chandra* X-ray survey of ejecta in the Cassiopeia A supernova remnant. *The Astrophysical Journal*, *746*(2), 130. https://doi.org/10.1088/0004-637x/746/2/130.

[7]Milisavljevic, D., Temim, T., & De Looze, I., et. al. (2024). A JWST survey of the supernova remnant Cassiopeia A. *The Astrophysical Journal Letters*, *965*(2). https://doi.org/10.3847/2041-8213/ad324b.

[8]Vink, J., Agarwal, M., & Slane, P., et. al. (2024). X-ray diagnostics of Cassiopeia A's "Green monster": Evidence for dense shocked circumstellar plasma. *The Astrophysical Journal Letters*, *964*(1). https://doi.org/10.3847/2041-8213/ad2fc5.

**Acknowledgments**

I would first like to thank Dr. Danny Milisavljevic for being an attentive, supportive, and guiding mentor through both my projects this summer. I would also like to thank graduate student Noah Zimmer for the immense help and mentorship in getting me into supernova dust science and supporting me throughout my second project.

Big thanks to Purdue for hosting this Summer 2025 REU program. Thank you to the NSF support from grants PHY-2244297, PHY-2209451 and AST-2206532, and NASA. I am grateful to Dr. Sergei Savikhin, Dr. Ian Arnold, Ms. Sonia Hill, and all the Purdue faculty and fellow REU constituents for making this summer possible.